The Astrophysical Journal, 891:63 (16pp), 2020 March 1 https://doi.org/10.3847/1538-4357/ab718e

The Structure of Radiatively Inefficient Black Hole Accretion Flows

Christopher J. White[1], Eliot Quataert[2], and Charles F. Gammie[3]
[1] Kavli Institute for Theoretical Physics, University of California Santa Barbara, Kohn Hall, Santa Barbara, CA 93107, USA; cjwhite@kitp.ucsb.edu
[2] Department of Astronomy, University of California Berkeley, 501 Campbell Hall, Berkeley, CA 94720, USA
[3] Department of Astronomy and Department of Physics, University of Illinois, Urbana, IL 61801, USA
Received 2019 September 30; revised 2020 January 11; accepted 2020 January 28; published 2020 March 4

Abstract

We run three long-timescale general-relativistic magnetohydrodynamic simulations of radiatively inefficient accretion flows (RIAFs) onto non-rotating black holes. Our aim is to achieve steady-state behavior out to large radii and understand the resulting flow structure. A simulation with adiabatic index $\Gamma = 4/3$ and small initial alternating poloidal magnetic field loops is run to a time of 440,000 GM/c^3, reaching inflow equilibrium inside a radius of 370 GM/c^2. Variations with larger alternating field loops and with $\Gamma = 5/3$ are run to 220,000 GM/c^3, attaining equilibrium out to 170 GM/c^2 and 440 GM/c^2. There is no universal self-similar behavior obtained at radii in inflow equilibrium: the $\Gamma = 5/3$ simulation shows a radial density profile with a power-law index ranging from -1 in the inner regions to $-1/2$ in the outer regions, while the others have a power-law slope ranging from $-1/2$ to close to -2. Both simulations with small field loops reach a state with polar inflow of matter, while the more ordered initial field has polar outflows. However, unbound outflows remove only a factor of order unity of the inflowing material over a factor of ∼300 in radius. Our results suggest that the dynamics of RIAFs are sensitive to how the flow is fed from larger radii, and may differ appreciably in different astrophysical systems. Millimeter images appropriate for Sgr A* are qualitatively (but not quantitatively) similar in all simulations, with a prominent asymmetric image due to Doppler boosting.

Unified Astronomy Thesaurus concepts: General relativity (641); Relativistic fluid dynamics (1389); Relativistic disks (1388); Low-luminosity active galactic nuclei (2033); Magnetohydrodynamical simulations (1966); Magnetohydrodynamics (1964); Accretion (14)

1. Introduction

A common mode of accretion onto black holes is that of a radiatively inefficient accretion flow (RIAF). Such systems have nonzero net angular momentum, as opposed to classical Bondi accretion (Bondi 1952), but because of inefficient cooling they are dynamically hot, thick disks (Ichimaru 1977; Rees et al. 1982; Narayan & Yi 1995), unlike standard thin-disk models (Shakura & Sunyaev 1973). RIAFs are consistent with a number of low-luminosity active galactic nuclei, including Sgr A* (Narayan et al. 1998).

Simulations of black hole accretion on horizon scales, where general relativity (GR) cannot be neglected, are almost always initialized as hydrostatic equilibrium torus solutions with simple angular momentum prescriptions (Fishbone & Moncrief 1976; Kozłowski et al. 1978; Chakrabarti 1985; Penna et al. 2013). While such simulations tend to reach a well-defined quasi-steady state in the inner portions of the flow, it is unknown how much this state depends on the fact that the simulations begin with a relatively artificial initial condition.

In thin accretion disks there is a large timescale separation between the viscous and dynamical times and rapid radiative cooling enables the flow to lose the memory of its initial thermodynamic state. This is much less true in RIAFs, so one might expect the dynamics of such flows to retain more memory of how the matter is fed to the vicinity of the black hole from larger radii. There are a number of analytic models for the structure of RIAFs, which differ primarily in the importance of non-radiative energy transport mechanisms, e.g., advection, convection/turbulence, and outflows (Narayan & Yi 1994; Blandford & Begelman 1999; Narayan et al. 2000; Quataert & Gruzinov 2000). It is unclear which, if any, of these is a correct description of RIAFs or whether different non-radiative energy transport mechanisms are important depending on how matter is fed to the vicinity of the black hole.

Previous work has shown that the flow structure at small radii in black hole accretion simulations depends on the magnetic field structure threading the initial torus, in particular how much magnetic flux there is at a given radius and/or through the whole torus (Narayan et al. 2003; Beckwith et al. 2008). The initial field structure influences both the strength of the resulting jet and whether the dominant angular momentum transport is produced by small-scale turbulent stresses due to the magnetorotational instability or by large-scale magnetic stresses.

One of the computational challenges of studying the connection between small- and large-scale flow structures is that the region in steady state grows outward only sublinearly with simulation time. Here we address this challenge with the brute-force method of long-timescale simulations that reach steady state over as extended a radial range as possible. We then attempt to address whether a well-defined self-similar state is reached at small radii independent of initial conditions.

The idea of running GR simulations for long times to achieve steady state over large distances has been pursued before, notably by Narayan et al. (2012).[4] They considered two instances of RIAF flows: a disk with standard and normal evolution (SANE), and a magnetically arrested disk (MAD). Their initial conditions differ only in whether the purely

[4] Stone et al. (1999), Igumenshchev & Abramowicz (2000), and Yuan et al. (2012) studied the radial structure of RIAFs using axisymmetric hydrodynamic simulations with an α viscosity, with outcomes differing with the details of that viscosity. The differences between hydrodynamic and magnetohydrodynamic (MHD) simulations make it difficult to know how to connect the results of those simulations to the MHD problem considered here.

poloidal magnetic field has the topology of a single loop in a slice of constant azimuth, conducive to accumulating net vertical magnetic flux and inducing a MAD state, or else has multiple loops and thus stays in the SANE regime. Their SANE simulation reaches steady state out to about 90 gravitational radii after running for a time $2 \times 10^5\, GM/c^3$.

Here we focus on the SANE case, primarily because such models are a priori more similar to the self-similar analytic models that still guide much of the intuition in thinking about RIAF structure across many decades in radius. We extend Narayan et al.'s (2012) work by running three variations on the initial conditions to probe how the final state is sensitive to details of the initial state, with the longest simulation run for a time $4.4 \times 10^5\, GM/c^3$. The numerics and setup of the simulations are detailed in Section 2. We present accretion rates and related global quantities in Section 3 and radial profiles of quantities in steady state in Section 4. The global inflow and outflow structure is analyzed in Section 5, and observational consequences are discussed in Section 6. Our conclusions are summarized in Section 7.

Throughout this work, all length scales will be expressed in implicit units of gravitational radii GM/c^2, where M is the black hole mass. Likewise, times are in units of GM/c^3 and velocities are in units of c, with units derived from these following naturally. The magnetic field contains an implicit factor of $1/\sqrt{4\pi}$, so, for example, the magnetic pressure is given by $p_{\rm mag} = \eta_{ij} B^i B^j/2$ if the components B^i are measured in a Minkowski frame comoving with the fluid.

2. Numerical Setup

We perform our simulations with the GRMHD code `Athena++` (White et al. 2016). The code uses a second-order van Leer integrator at a Courant–Friedrichs–Lewy number of 1/4, where 1/2 is the maximum stable value for this integrator in three spatial dimensions, along with second-order modified van Leer spatial reconstruction from Mignone (2014). Fluxes are calculated via the HLLE Riemann solver.

While less diffusive Riemann solvers such as HLLD exist for relativistic MHD (Mignone et al. 2009), we choose HLLE based on two considerations. First, shocks in HLLD are narrowed to be only one or two cells thick. In a multi-dimensional finite-volume method, such steep gradients can lead to the conserved variables in a cell entering a physically inadmissible state during a single time step, manifesting as a variable inversion failure when trying to recover the primitive variables. Given that these simulations need to take tens of millions of time steps, we want to minimize the chance of catastrophic inversion failures. Second, HLLE is common practice in the GRMHD community. For example, in the recent code comparison of Porth et al. (2019), which includes `Athena++`, the nine codes exclusively employ either HLLE or the more diffusive LLF Riemann solver, yet they are able to reach agreement with sufficient resolution. HLLD would enable us to resolve the same phenomena with fewer cells, but we are willing to use HLLE with higher resolution here in order to achieve robustness over very long integration times.

Spacetime is fixed to be that of a nonspinning black hole, $a = 0$. The simulations employ spherical Kerr–Schild coordinates (t, r, θ, ϕ) with volume element $\sqrt{-g} = r^2 \sin\theta$. Our coordinate system covers the entire sphere, including the appropriate transmissive polar boundary. In the radial direction the cell boundaries are logarithmically spaced from $r = 1.7$ (inside the horizon) to $r = 10^4$. In the poloidal direction we compress the cells near the equatorial plane as in Gammie et al. (2003) (except we adjust cell spacing rather than the metric). The result is that cells are uniformly spaced in a midplane-compressed coordinate $\theta_{\rm c}$ related to the standard θ via

$$\theta = \theta_{\rm c} + 0.35 \sin(2\theta_{\rm c}). \tag{1}$$

Due to the particularly long integration times required for these simulations, we additionally use static mesh refinement to keep the part of the grid near the poles at low resolution. The root grid consists of $120 \times 20 \times 20$ cells in the radial, polar, and azimuthal directions respectively. The region $\pi/5 < |\theta_{\rm c} - \pi/2| < 3\pi/10$ is refined by a factor of 2 in each dimension, and the region $|\theta_{\rm c} - \pi/2| < \pi/5$ is refined by a factor of 4 relative to the root grid. The cells at the midplane thus have thickness $\Delta\theta \approx 0.0118 \approx \pi/266$.

The initial conditions are those of the hydrostatic equilibrium solution of Fishbone & Moncrief (1976) with a pressure maximum at $r = 52$ and a peak density of $\rho = 1$. The latter sets an arbitrary scale for the fluid mass, which is taken to be negligible compared to the black hole mass. Simulations A and B have an inner edge at $r = 25$ and an adiabatic index of $\Gamma = 4/3$, while simulation C has an inner edge at $r = 25.1$ and $\Gamma = 5/3$. Indices of $\Gamma = 4/3$ and $\Gamma = 5/3$ are approximations to the thermodynamics appropriate for super- and sub-Eddington RIAFs, respectively. The slight change of inner edge radii helps to make the extent of the mass distribution of simulation C similar to that of the other two. The resulting densities are shown in Figure 1, with the midplane run of ρ with radius on the top and a vertical slice on the bottom.

We add a weak magnetic field to this initial torus. The field is derived from the purely azimuthal vector potential with component

$$A_\phi \propto (\max(p_{\rm gas} - p_{\rm gas,min}, 0))^{1/2}\, r^2 \sin(\theta) \times \sin\left(\pi N_r L(r;\, r_{\rm min},\, r_{\rm max})\right) \sin\left(\pi N_\theta L(\theta;\, \theta_{\rm min},\, \theta_{\rm max})\right), \tag{2}$$

where $p_{\rm gas}$ is the gas pressure and L is a linear ramp function:

$$L(x;\, x_{\rm min},\, x_{\rm max}) = \begin{cases} 0, & x \leqslant x_{\rm min}; \\ \dfrac{x - x_{\rm min}}{x_{\rm max} - x_{\rm min}}, & x_{\rm min} < x < x_{\rm max}; \\ 1, & x \geqslant x_{\rm max}. \end{cases} \tag{3}$$

The form of this function is chosen to allow for a variable number of counterrotating loops in both directions, and to give roughly constant values for plasma $\beta^{-1} \equiv p_{\rm mag}/p_{\rm gas}$, the ratio of magnetic to gas pressure. We choose the parameters $p_{\rm gas,min} = 10^{-8}$, $r_{\rm min} = 30$, $r_{\rm max} = 1000$, $\theta_{\rm min} = \pi/6$, and $\theta_{\rm max} = 5\pi/6$ in all simulations. For simulations A and C we have $N_r = 6$ and $N_\theta = 4$, while in simulation B we set $N_r = 6$ and $N_\theta = 1$. In all cases the field strength is normalized such that

$$\frac{\int \beta^{-1} \rho \sqrt{-g}\; dr\, d\theta\, d\phi}{\int \rho \sqrt{-g}\; dr\, d\theta\, d\phi} = 10^{-2}, \tag{4}$$

where the integrals exclude the background atmosphere outside the torus. These field configurations are illustrated in Figure 2.

Finally, we perturb the initial velocities inside the torus as follows. We consider the normal observer velocity components $u^{i'} \equiv u^i + \beta^i u^0$, where β^i is a component of the standard 3 + 1

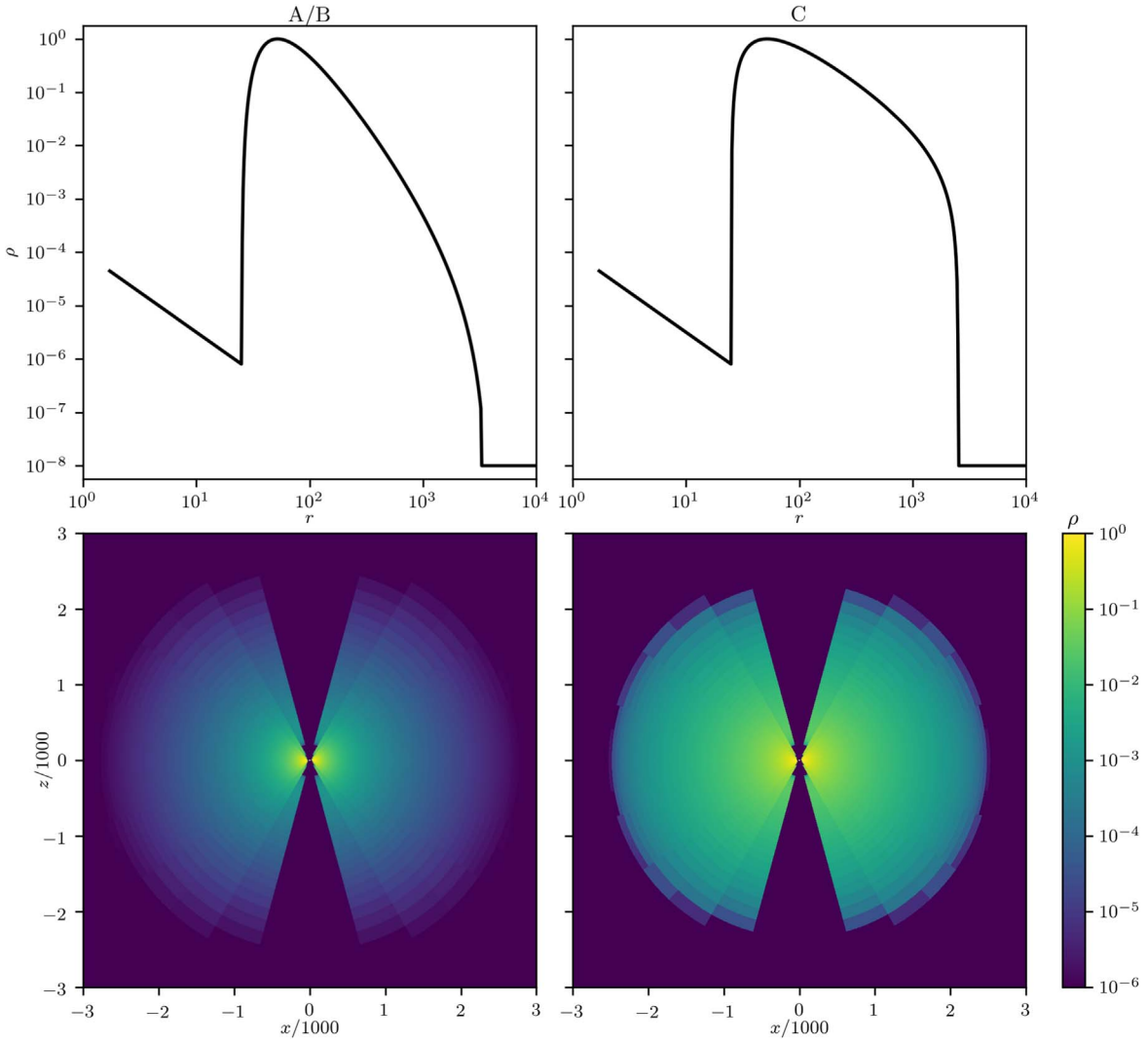

Figure 1. Density ρ for the hydrostatic equilibrium initial conditions. The left panels show the setup for simulations A and B, while the right panels show simulation C. Midplane values as a function of radius are shown on top, with a vertical slice in the xz-plane shown on the bottom. The power-law floor is a background atmosphere inserted for numerical purposes.

shift. We introduce small motions in the poloidal directions according to

$$\Delta u^{1'} = \Delta_0 \frac{R}{r} u^{3'} \sin(k_R R)\cos(k_z z), \tag{5a}$$

$$\Delta u^{2'} = \Delta_0 \frac{z}{r^2} u^{3'} \sin(k_R R)\cos(k_z z), \tag{5b}$$

where $R = r\sin\theta$ and $z = r\cos\theta$ are standard cylindrical coordinates. We choose $\Delta_0 = 0.03$ and k_R, $k_z = \pi/50$.

Simulation A is run to $t = 4.4 \times 10^5$, while variations B and C are run to $t = 2.2 \times 10^5$. The cost of these runs is approximately 1.1 core-hours per simulation time unit (Intel Xeon E5-2670 CPU) or 0.7 core-hours per time unit (Intel Xeon Platinum 8160 CPU).

3. Accretion Rates

We follow Narayan et al. (2012) and divide the simulations into logarithmic chunks in time. The eight boundaries of these seven chunks are 3.89×10^4, 5.5×10^4, 7.78×10^4, 1.11×10^5, 1.556×10^5, 2.2×10^5, 3.111×10^5, and 4.4×10^5. We will use a consistent color scheme to label these chunks throughout all figures.

The mass accretion rate is defined in the usual way, integrating over a spherical shell:

$$\dot{M} = -\oint \rho u^1 \sqrt{-g}\, d\theta\, d\phi. \tag{6}$$

The run of the horizon value of $\dot{M}$ with time is given in Figure 3. As can be seen in the figures, the first time chunks are chosen to be well after the initial transience. Simulations A and B begin depleting their mass reservoir, while simulation C has much more mass and thus only shows signs of decreasing $\dot{M}$ at the very end of the run. By the end of chunk 5 ($t = 2.2 \times 10^5$), simulations A, B, and C have lost 29%, 19%, and 12% of their initial masses, with 15%, 7.0%, and 9.5% of the original mass going through the horizon. After simulation A has run for twice as long, it has lost a total of 61% of its mass, with 17% going into the black hole. Some of this mass

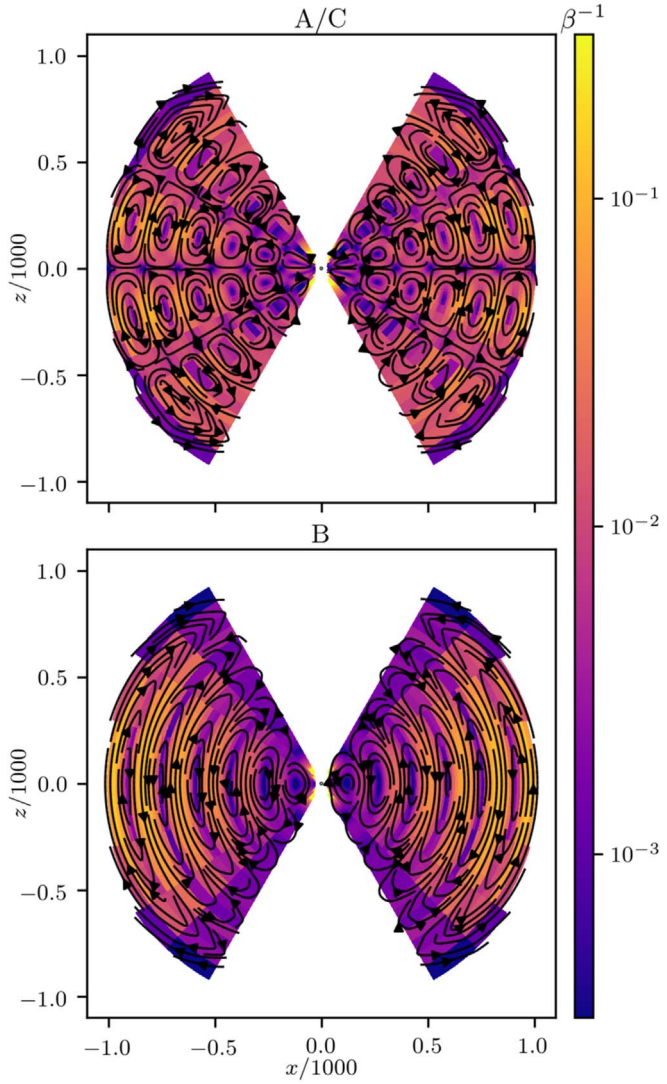

Figure 2. Initial magnetic field configurations for simulations A and C (top) and simulation B (bottom). The streamlines show the poloidal field loops, and the background color is plasma β^{-1}. While both configurations have no net vertical flux when averaged over sufficiently large volumes, only the one on top has no net vertical flux on any shell of constant radius. Note that the scale of these images is different from that in Figure 1; the initial field does not fill the entire torus.

loss is due to bulk outflows originating from smaller radii (discussed in Section 5), while the rest comes from the outer parts of the initial torus moving outward as they receive angular momentum from the inner parts. In simulation A, the accretion rate approaches a scaling of $\dot{M} \sim t^{-4/3}$ at very late times, as shown by the dotted line. This is the expected scaling for a RIAF in the absence of outflows removing mass or angular momentum. Since the simulation has outflows and is probably not fully in the asymptotic regime where $t^{-4/3}$ would be expected, it seems likely that the agreement between the simulation and this analytic expectation is fortuitous.

We can also look at $\dot{M}$ as a function of radius. This is done in Figure 4, where the separate lines are time averages over different chunks. In steady state we expect these values to be close to constant out to some radius, and indeed they are even as this constant decreases with time. The flatness of the curves at the inner radii indicates the solution is in a quasi-steady state and that numerical density floors do not play a large role in the inner parts of the simulations.

For later analysis, we use the $\dot{M}$ versus radius curves to define a "viscous radius" inside of which the system has reached inflow equilibrium. We choose the point where $\dot{M}$ drops to $e^{-1/2}$ times its horizon value. These radii are delineated by the points in Figure 4. The range over which equilibrium is established does indeed move outward in time, extending to $r = 370$ in chunk 7 of simulation A and to $r = 170$ and $r = 440$ in chunk 5 of simulations B and C. For a constant h/r and constant α model we would expect the viscous radius to move outward in time as $t^{2/3}$. The numerical evolution is generally slower than this, as we discuss further below in Section 4.

The energy accretion rate is very similar to the total mass accretion rate. Define

$$\dot{E} = \oint T^1{}_0 \sqrt{-g}\, d\theta\, d\phi, \tag{7a}$$

$$\dot{E}_{\rm mag} = \oint (T_{\rm mag})^1{}_0 \sqrt{-g}\, d\theta\, d\phi, \tag{7b}$$

where the stress-energy tensor is given by

$$T^{\mu\nu} = T^{\mu\nu}_{\rm gas} + T^{\mu\nu}_{\rm mag}, \tag{8a}$$

$$T^{\mu\nu}_{\rm gas} = \left(\rho + \frac{\Gamma}{\Gamma - 1} p_{\rm gas}\right) u^\mu u^\nu + p_{\rm gas} g^{\mu\nu}, \tag{8b}$$

$$T^{\mu\nu}_{\rm mag} = 2 p_{\rm mag} u^\mu u^\nu + p_{\rm mag} g^{\mu\nu} - b^\mu b^\nu, \tag{8c}$$

$$p_{\rm mag} = b_\lambda b^\lambda / 2, \tag{8d}$$

$$b^0 = u_i B^i, \tag{8e}$$

$$b^i = \frac{1}{u^0}(B^i + b^0 u^i). \tag{8f}$$

Runs of $\dot{E}$ and $\dot{E}_{\rm mag}$ with radius, averaged in time over chunk 5, are shown in Figure 5. The other time chunks show essentially the same behavior. The overall energy accretion rate tracks mass very closely. This is to be expected, since rest mass density ρ dominates over gas pressure $p_{\rm gas}$, as well as the contribution of the electromagnetic field. That is, we are mostly measuring rest mass being advected into the black hole. The electromagnetic contribution to the flux of energy, shown by the dotted line, is negative, indicating an outflow. However the magnitude of this component is only one part in a thousand of the total. This would be significantly larger for a spinning black hole.

Just as with mass and energy we monitor the flux of angular momentum, defining

$$\dot{J} = -\oint T^1{}_3 \sqrt{-g}\, d\theta\, d\phi. \tag{9}$$

This is also shown in Figure 5. Again we see the radially constant plateaus indicating approximate steady state, though the deviations begin at slightly smaller radii than for $\dot{M}$. The steady-state value of $\dot{J}/\dot{M}$ does not change with magnetic field topology (see simulations A and B), but does change in the case of a different Γ (simulation C).

We additionally calculate the horizon-penetrating flux

$$\varphi = \frac{\sqrt{4\pi}}{2\dot{M}^{1/2}} \oint_{r=r_{\rm hor}} |B^1| \sqrt{-g}\, d\theta\, d\phi. \tag{10}$$

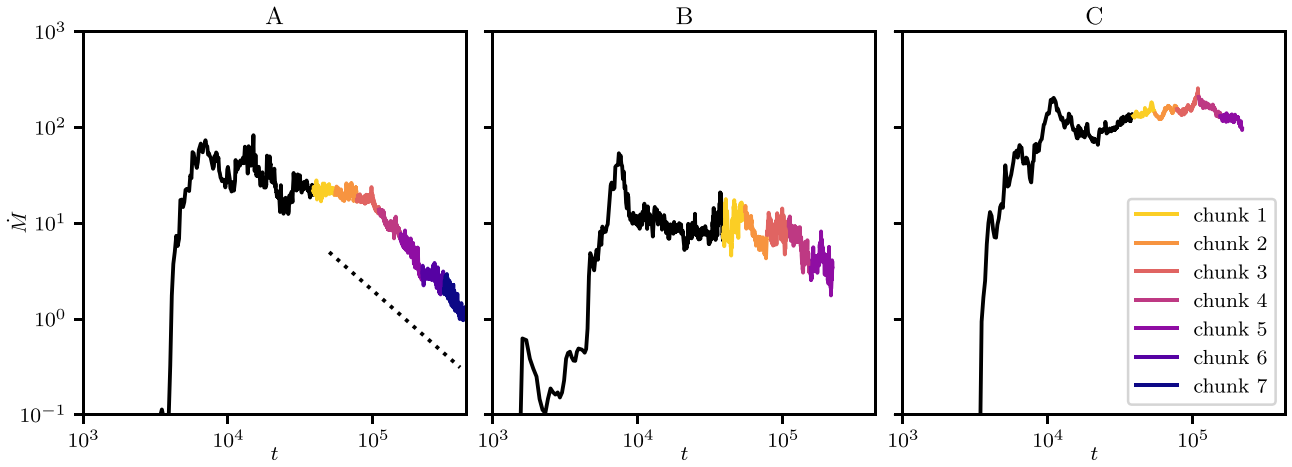

Figure 3. Horizon accretion rates as functions of time. The time chunks used for later analysis are indicated by the colors, where even the earliest chunk begins well after the sudden spike in accretion that is a remnant of the initial conditions. Simulation C begins with more mass than the other two, so the torus does not begin to significantly deplete over the course of the simulation, despite the higher accretion rate. The dotted line indicates the slope of a power law going as $t^{-4/3}$.

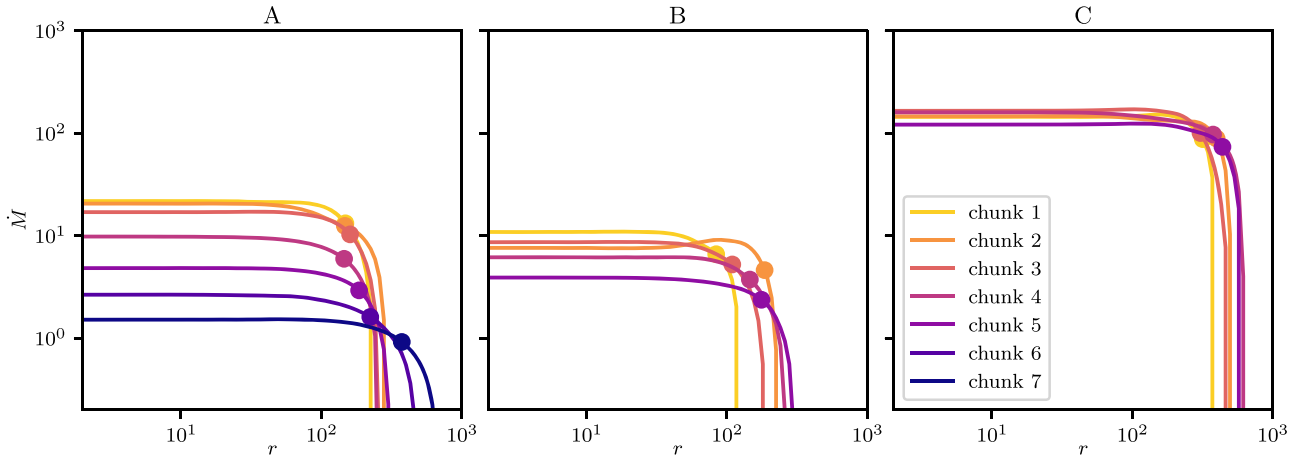

Figure 4. Time-averaged mass accretion rates as functions of radius. Level portions of the curves indicate the establishment of inflow equilibrium. The points denote the outer edges of nominal viscous ranges, which are extending outward as time progresses in all simulations.

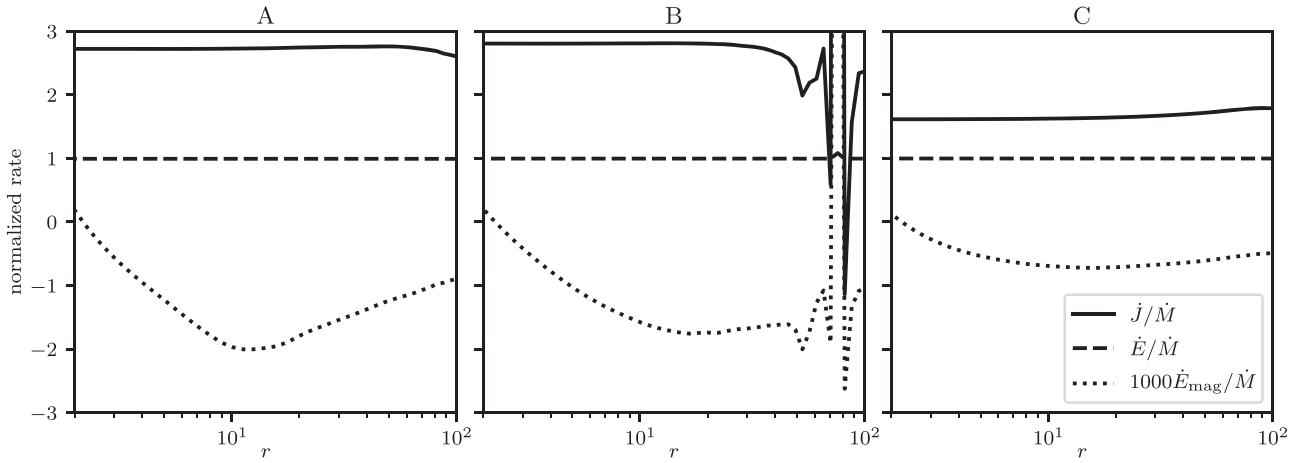

Figure 5. Time-averaged energy and angular momentum accretion rates as functions of radius. In all cases the rates are normalized by the horizon value of $\dot{M}$ before being averaged in time over the fifth time chunk ($1.556 \times 10^5 \leqslant t < 2.2 \times 10^5$). Both $\dot{J}$ and $\dot{E}$ should be constant in steady state, as they are, with $\dot{E}/\dot{M} \approx 1$ indicating rest mass advection dominates the energy budget. Electromagnetic energy outflow is a small fraction of the total (a consequence in part of our use of nonspinning black holes). The negative sign of $\dot{E}_{\rm mag}$ corresponds to outflow of energy as measured at infinity.

This is the same quantity as $\phi_{\rm BH}$ defined in Tchekhovskoy et al. (2011) and Narayan et al. (2012), where our explicit factor of $\sqrt{4\pi}$ is implicit in their units, except here we use the instantaneous $\dot{M}$ not convolved with any smoothing kernel in time. The run of φ with time in the two simulations is shown in Figure 6. Simulations A and C, with their small initial field

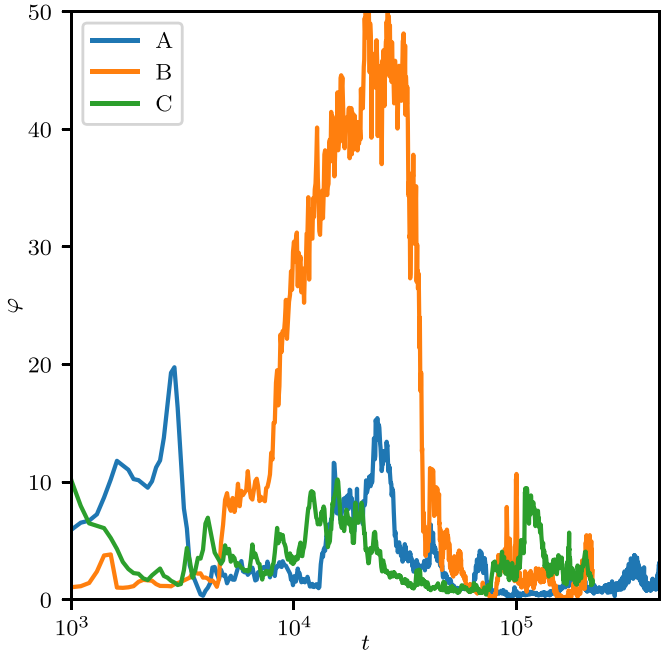

Figure 6. Horizon-penetrating magnetic fluxes as functions of time. Simulation B does not stay in a MAD state, but it does build up more coherent flux than simulations A and C. This is not unexpected given the initial conditions (Figure 2), where each radius in simulation B has net vertical flux, while those in simulations A and C do not.

loops (see Figure 2), stay very much in the SANE regime, with $\varphi \lesssim 10$ at late times. For comparison, the MAD simulations in Tchekhovskoy et al. (2011) have $\varphi \approx 47$. Simulation B goes through a burst of higher flux, though it does not stay high as in a true MAD disk. The behavior of simulation B matches that of the SANE simulation in Narayan et al. (2012), which uses a similar initial field topology.

4. Radial Profiles in the Disk

We now turn to characterizing the properties of the disks, starting with profiles of disk properties as functions of radius.

We define the spherical scale height at a radius to be

$$\frac{h}{r} = \tan\left(\frac{\oint |\theta - \pi/2|\ \rho\sqrt{-g}\ d\theta\ d\phi}{\oint \rho\sqrt{-g}\ d\theta\ d\phi}\right), \tag{11}$$

where the integrals are taken over spheres at that radius. The run of this quantity with radius, averaged within time chunks, is shown in Figure 7. In all simulations, this scale height stays between approximately 0.1 and 0.7, increasing toward larger radii and changing little over time. Simulation C, with $\Gamma = 5/3$, stays somewhat thicker at very small radii compared to the other cases.

With scale height in hand, we can define averages of quantities over the disk proper, here taken to be the region within one scale height of the midplane. The average density we define is

$$\langle \rho \rangle = \frac{\int_{\rm disk} \rho\sqrt{-g}\ d\theta\ d\phi}{\int_{\rm disk} \sqrt{-g}\ d\theta\ d\phi}. \tag{12}$$

Note that a more appropriate volume element might use the determinant of the metric restricted to $2+1$ hypersurfaces of constant r, or even $2+0$ surfaces of constant t and r. However, all these choices differ by factors that depend only on r in the case of nonspinning black holes, so they all lead to equivalent definitions of $\langle \rho \rangle$.

The profiles of density are shown in the upper panels of Figure 8, where the points indicate inflow equilibrium as defined in Section 3. The profiles generally approach power laws in radius, especially at very late times in simulation A. The very inner regions of simulations A and B, inside $r \approx 10$, have a shallower power-law slope when compared with the outer part of the viscous range. This is likely produced by the rapid acceleration needed close to the horizon: conservation of mass implies that the density profile flattens as the velocity accelerates. Somewhat surprisingly, simulation C does not display this knee, though it does have a slight persistent kink between $r = 50$ and $r = 100$.

The lower panels of Figure 8 show the power-law slopes of the density profiles. Specifically, for an abscissa r_0 the ordinate is the slope of a linear regression to the set of points $(\log r, \log \langle \rho \rangle)$ for which r is within a factor of approximately 2 of r_0. The inner regions of simulations A and B have slopes of very roughly $-1/2$. The range over which this holds does not increase after a point, even at very late times, as in simulation A. The middle of the inflow equilibrium range in simulation A eventually tends toward a slope of approximately $-3/2$ at very late times. Simulation B does not reach sufficiently late times and does not show signs of converging to a constant slope. Simulation C, on the other hand, has a slope of between $-1/2$ and -1 over all radii in equilibrium. Analytic models of RIAFs predict power-law density profiles far from the horizon ranging from $r^{-3/2}$ (Narayan & Yi 1994) to $r^{-1/2}$ (Narayan et al. 2000; Quataert & Gruzinov 2000), and everything in between (Blandford & Begelman 1999). One might expect that there would be a well-defined self-similar state of the accretion flow that obtains at radii $r \gg 1$, where the impact of the black hole horizon on the flow structure is no longer significant. The density profiles in Figure 8 are not consistent with this ansatz. Instead, the profiles depend on the thermodynamics, parameterized by adiabatic index here, and initial magnetic field structure.

We can average other quantities in a density-weighted way. For any quantity q other than ρ, define

$$\langle q \rangle = \frac{\int_{\rm disk} q\rho\sqrt{-g}\ d\theta\ d\phi}{\int_{\rm disk} \rho\sqrt{-g}\ d\theta\ d\phi}. \tag{13}$$

Although not shown explicitly here, all three accretion flows are slightly sub-Keplerian, as can be seen by examining $\langle \Omega \rangle$ for Boyer–Lindquist angular velocity $\Omega = u^3_{\rm BL}/u^0_{\rm BL}$. The average infall velocity $-\langle v^r \rangle$, where $v^r = u^1/u^0$, is well below the freefall value.

The averages of magnetization $\langle \beta^{-1} \rangle$ are given in Figure 9. Magnetization decreases with increasing radius out to $r \approx 25$ in all simulations, but it remains relatively flat beyond that in cases A and B, even when equilibrium is established much further out. The levels of these flat portions can change in time, however, first decreasing and then increasing at late times (simulation A). We note that simulations A and B, whose only difference is the initial field topology, reach the same profile of

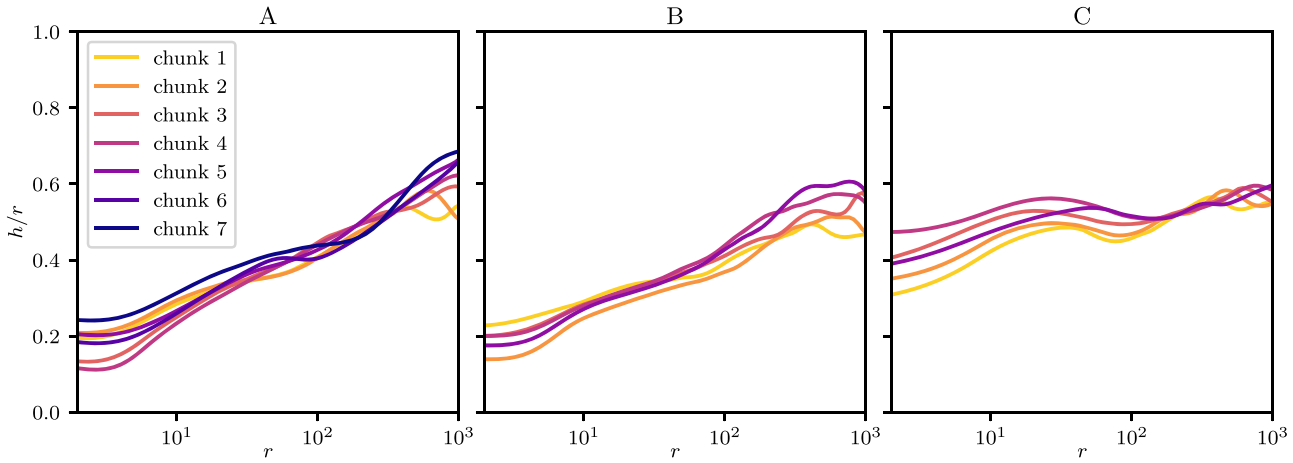

Figure 7. Time-averaged scale heights as functions of radius. The disks have roughly the same thicknesses in all three cases, though simulation C is somewhat more spherical overall (see also Figure 10). The scale heights do not change much over time.

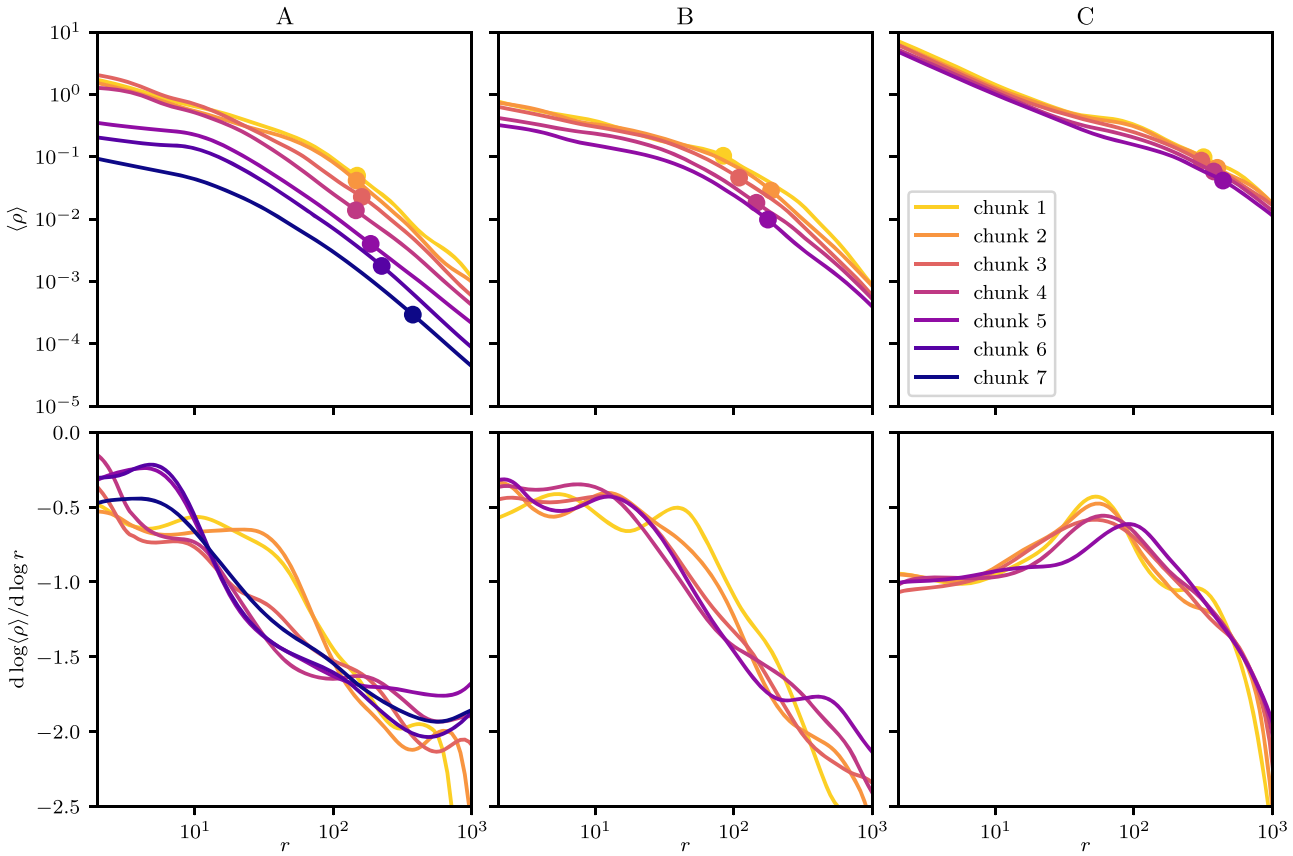

Figure 8. Density profiles in radius, averaged over the disk and averaged over time chunks. The profiles themselves are displayed in the top panels, with their power-law slopes shown below. The points are at the same viscous radii as in Figure 4. Simulations A and B show shallower slopes inside $r \approx 10$ compared to farther out, while simulation C has an intermediate slope at small radii and a shallow plateau at intermediate radii. There is no convergence to a well-defined density profile at intermediate radii (between the ISCO and viscous radii), as one might expect if the solutions were approaching a self-similar RIAF solution.

$\langle \beta^{-1} \rangle$ by the fourth time chunk, indicating that the saturated field strength may not strongly depend on details of initial conditions. In simulation C, the profile of $\langle \beta^{-1} \rangle$ levels off near where $\langle \rho \rangle$ does, and then proceeds to again decrease with increasing radius beyond that.

The increased magnetization at small radii influences the rates at which our viscous radii move outward. Given the scaling $t_{\rm visc} \sim r^{3/2}(h/r)^{-2}$, and given the observed thicknesses $h/r \sim r^{1/4}$ (Figure 7), we might expect equilibrium to be established out to a radius $r_{\rm visc} \sim t$ by time t. However, the radii marked in Figure 4 do not advance in time this rapidly. For example, chunks 1 and 7 are separated by a factor of 8 in time, while equilibrium is only established 2.5 times farther out in the latter compared to the former for simulation A. This can be explained by noting we also expect $t_{\rm visc} \sim \alpha^{-1}$, and $\alpha \sim \beta^{-1}$. Thus, $r_{\rm visc} \sim \beta^{-2/3} t$, and thus equilibrium is established much more rapidly at small radii with strong magnetization than at large radii.

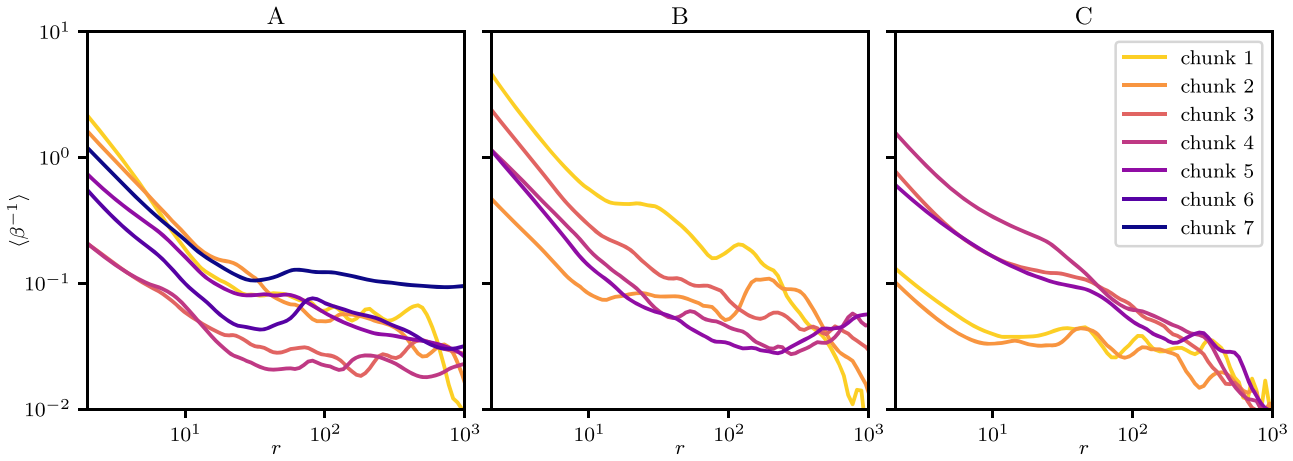

Figure 9. Profiles of magnetic-to-gas pressure ratios in radius, averaged in a density-weighted way over the disk and then averaged over time chunks. In all cases the magnetization steeply declines with radius in the inner parts of the disk and tends to level off at large radii. Note that the trends with time are not necessarily monotonic.

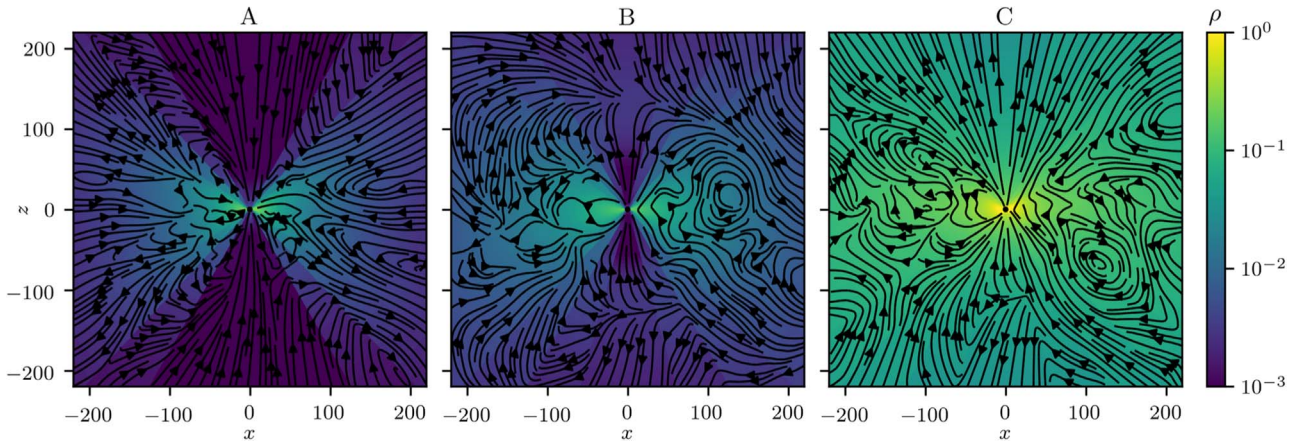

Figure 10. Average late-time (chunk 5, $1.556 \times 10^5 \leqslant t < 2.2 \times 10^5$) poloidal magnetic field, with background color indicating average density. Simulation A displays a more coherent radial field in the disk than the other two. Additionally, the symmetric/antisymmetric character of B^z across the midplane $z = 0$ follows from the character of the initial fields, shown in Figure 2. The density structure in simulation C is quite spherically symmetric compared to the equatorial disk and evacuated polar region seen in simulation A.

5. Global Structure of the Accretion Flow

Going beyond radial profiles, we show the late-time magnetic field in the poloidal plane in Figure 10, superimposed on the time-averaged density. This magnetic field is obtained by averaging B^1 and B^2 in azimuth and averaging in time over the last common time chunk (5) available for all simulations. It shows what steady-state structure arises from the initial fields in Figure 2.

We can immediately see that simulation A has a more ordered, radial field near the midplane when compared to the other two cases, despite simulation C having the same initial field topology. This can be explained by the velocity structure of the flows, as discussed below. Simulation A also shows near cancellation in vertical fluxes at fixed radius; i.e., B^z is antisymmetric across $z = 0$. Simulation B, on the other hand, shows a field topology with B^z symmetric across the midplane. While the net flux integrated over a large radial extent may vanish, there is generally net flux at any given radius. These symmetries are also found in the initial conditions, indicating that even at these late times the initial field's imprint on the field topology remains. It is also striking how spherical the density distribution is in simulation C: there is variation by only a few factors in density from equator to pole. By contrast, simulations A and B show the more "standard" disk structure of a dense midplane and a low-density polar region.

The net accretion rates shown in Figures 3 and 4 do not fully describe the radial motion of matter, since there can be outflows partially negating mass inflow elsewhere. While this will certainly happen over small time and length scales due to turbulence, coherent outflows may persist even when averaged over turbulence.

We observe large-scale outflows in our simulations, particularly with more ordered magnetic fields. Figure 11 shows the velocity field for each simulation in the poloidal plane, averaged in azimuth with density weighting and again averaged over the last common time chunk. Simulation B shows an accretion disk with a low radial velocity, together with fast, low-density, polar outflows. This is similar to the now canonical assumed structure of RIAFs from earlier simulations (e.g., Hawley & Balbus 2002). Simulations A and C, however, show the reverse. In these cases matter is falling in through the poles, with outflow occurring in the disk. This disk outflow pattern is particularly strong in simulation A.

We can further decompose $\dot{M}$ into incoming and outgoing components based on radial mass fluxes that have been

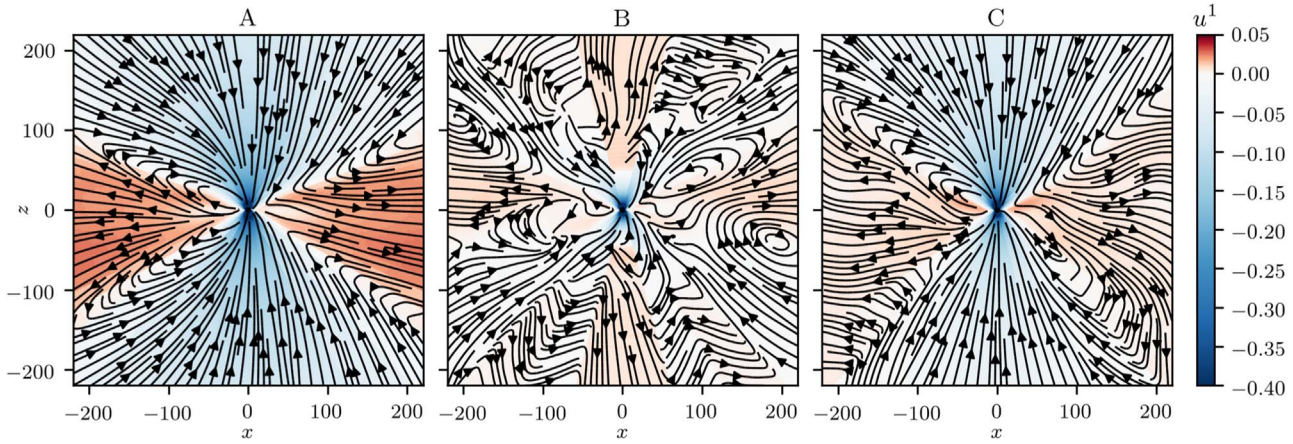

Figure 11. Average late-time (chunk 5, $1.556 \times 10^5 \leqslant t < 2.2 \times 10^5$) poloidal velocity field in the simulations. The background colors highlight the radial velocity, with blue indicating inflow. Simulations A and C display polar inflows with outflows in the disk, while simulation B has polar outflows and at least some disk inflow.

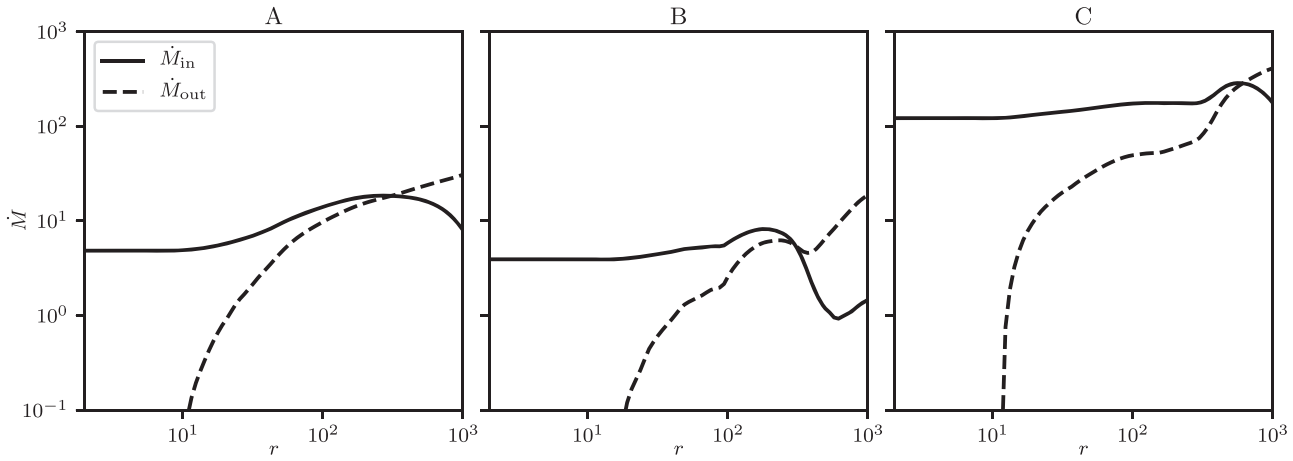

Figure 12. Bulk ingoing and outgoing mass fluxes at late times (chunk 5, $1.556 \times 10^5 \leqslant t < 2.2 \times 10^5$) in the simulations. Over the viscous range, inflow is relatively constant, while outflow is less in magnitude and decreases inward. Over the factor of ∼300 in radius that our solutions are in viscous equilibrium, the total outflow rate is only comparable to the inflow rate. There is no bulk outflow inside $r \approx 10$, indicating that this is inside the stagnation radius of any polar outflows (simulation B, see Figure 11). Note that the incoming and outgoing mass fluxes necessarily combine to the net inflow rates shown in Figure 4.

averaged in time and azimuth:

$$\dot{M}_{\rm in} = -2\pi \int_0^\pi \min(\langle \rho u^1 \rangle, 0) \sqrt{-g}\, d\theta, \tag{14a}$$

$$\dot{M}_{\rm out} = 2\pi \int_0^\pi \max(\langle \rho u^1 \rangle, 0) \sqrt{-g}\, d\theta. \tag{14b}$$

The runs of these quantities with radius are given in Figure 12. We know $\dot{M}_{\rm in}$–$\dot{M}_{\rm out}$ must be constant in radius from Figure 4, and $\dot{M}_{\rm in}$ is close to constant, with $\dot{M}_{\rm out}$ being a small perturbation over most of the viscous range. The fact that $\dot{M}_{\rm out}$ becomes negligible inside $r \approx 10$ in simulations A and C tells us that the disk outflows we observe (see Figure 11) do not extend all the way to the horizon. In simulation B, $\dot{M}_{\rm out}$ also drops off at small radii, matching how the polar outflow shown in Figure 11 reaches a stagnation surface at $r \approx 25$. Our results on the disk outflows are broadly consistent with Narayan et al. (2012), who also find that outflows were at most an order unity perturbation to the accretion rate for the radial range they simulate.

What is the physical origin of the outflows seen in Figure 12 and the flow structure seen in Figure 11? Two possible hydrodynamic mechanisms for large-scale flows of this kind are convection and meridional circulation. We examine these quantitatively in Appendix A and find that they are not very compelling for explaining our numerical results.

The fact that both simulations A and C display polar inflows and disk outflows despite having different values of Γ and different initial tori indicates this phenomenon is not limited to a small set of hydrodynamic initial conditions. Simulations A and B, meanwhile, have identical hydrodynamic initial conditions yet vastly different steady-state velocity structures. This points to the original magnetic field topology as being important in determining the inflow and outflow structure (as was emphasized by, e.g., Beckwith et al. 2008).

As discussed in Section 2, the initial field in simulation B consists of elongated loops in the poloidal plane (see Figure 2). While there is no net vertical flux when averaged over sufficiently large radial extents, there is net flux at any given radius. Thus accretion brings a sequence of alternating net fluxes to the black hole over time (Figure 6), causing bursts in accretion rate (Figure 3). While the black hole has no spin and thus there are no Blandford–Znajek jets (Blandford & Znajek 1977), the net flux in the disk may be enough to drive a polar outflow via the Blandford–Payne mechanism (Blandford & Payne 1982) or related MHD processes. This can

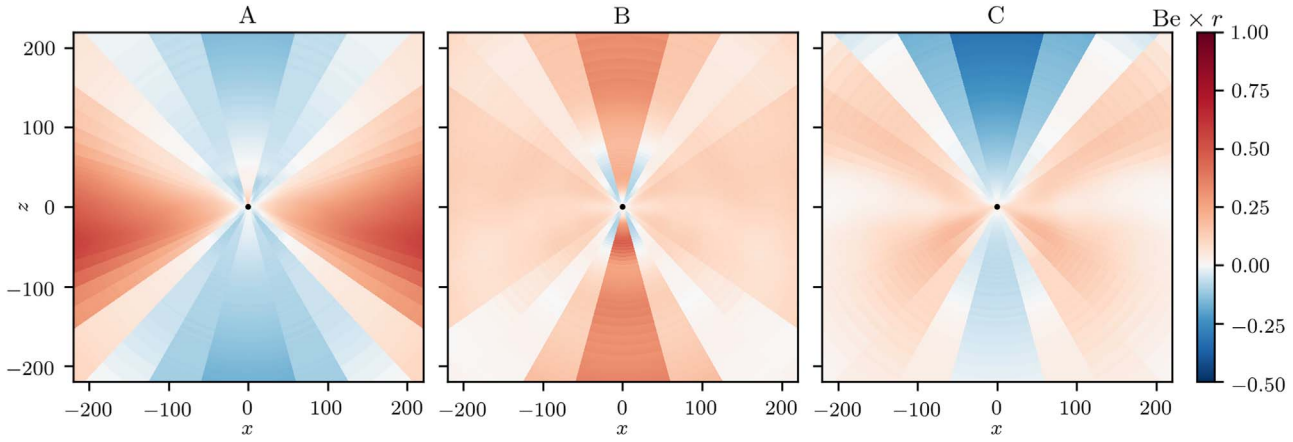

Figure 13. Average Bernoulli parameter (see Equation (15)) in the simulations, calculated in the fifth time chunk ($1.556 \times 10^5 \leqslant t < 2.2 \times 10^5$). Only in simulation B is the polar region unbound. The disks have largely become unbound, despite the fact that the initial conditions are bound everywhere with negative Bernoulli parameter.

prevent any loosely bound polar inflow coming in from the disk at larger radii from reaching the black hole.

Simulations A and C, on the other hand, have no net flux at any radius. It is more difficult for the magnetic field in these cases to launch polar outflows, so material can fall to the black hole near the polar axes. With enough polar inflow, the liberated gravitational potential energy can help to unbind material, driving it outward in the equatorial plane.

We quantify the extent to which material is bound with the Bernoulli parameter, which we define as

$$\mathrm{Be} \equiv -\frac{\langle w u_0 \rangle}{\langle \rho \rangle} - 1, \tag{15a}$$

$$w \equiv \rho + \frac{\Gamma}{\Gamma - 1} p_{\mathrm{gas}} + 2 p_{\mathrm{mag}}, \tag{15b}$$

with averages being taken in azimuth and time. This is similar to Equation (11) of Narayan et al. (2012). Plots of Be for the last common time chunk of each simulation are given in Figure 13. Note $\mathrm{Be} < 0$ throughout the initial tori.

We see that most of the disks in all three cases have become unbound. At the same time, the polar regions of simulations A and C are bound, while they are very much unbound in simulation B. The initial magnetic field topology thus has a strong effect on the overall energetics and dynamical structure of RIAFs. This occurs primarily, we believe, via the energy redistribution and outflows associated with magnetic stresses, not just the angular momentum transport they produce.

Evidence for this comes from the fact that over a large range of radii all three simulations have similar radial accelerations, vanishing near the midplane and directed inward at high latitudes. The presence of a narrow outflow along the polar axis, for instance, is not due to consistent, outward, electromagnetic acceleration along the axis, but rather to the combined effect of accelerations at other locations. We quantify these accelerations by writing the inhomogeneous geodesic equation for a perfect fluid as

$$\frac{du^\mu}{d\tau} = f^\mu_{\mathrm{grav}} + f^\mu_{\mathrm{gas}} + f^\mu_{\mathrm{EM}}, \tag{16a}$$

$$f^\mu_{\mathrm{grav}} = -\Gamma^\mu_{\alpha\beta} u^\alpha u^\beta, \tag{16b}$$

$$f^\mu_{\mathrm{gas}} = -\frac{1}{w} P^{\mu\alpha} \nabla_\alpha p_{\mathrm{gas}}, \tag{16c}$$

$$f^\mu_{\mathrm{EM}} = -\frac{1}{w} P^{\mu\alpha} (\nabla_\alpha p_{\mathrm{mag}} - \nabla_\beta (b_\alpha b^\beta), \tag{16d}$$

where $P^{\mu\alpha} = g^{\mu\alpha} + u^\mu u^\alpha$ is the projection operator relative to the fluid velocity. Figure 14 shows the radial components of these three forces along an arc of constant radius $r = 50$, computed from the fluid state obtained by averaging in time and azimuth over chunk 5. The gravitational (including centrifugal) force is closely balanced by the gas pressure gradient; the magnetic pressure gradient and Maxwell stress are both small. In simulation A but not in simulation C, there may be some ongoing outward radial acceleration near the upper and lower disk surfaces. In these locations f^1_{grav} approaches 0, indicating a large centrifugal force nearly balancing gravitational attraction even without pressure support.

Appendix B shows the steady-state behavior of two additional runs, paralleling simulations A and B in how their initial fields differ but using a smaller initial torus. The dichotomy between polar inflows and outflows persists, with inflows occurring where there is no local net vertical flux in the initial conditions. These smaller tori, which are closer in size to those most often employed in the literature, are more tightly bound, so even the case with polar inflow does not develop an equatorial outflow. The latter result highlights that conclusions drawn from small torus simulations might be inaccurate in some cases.

6. Observational Consequences

Given the length of time we have run these simulations, we have a large amount of data on their time variability. In particular, for simulation A we have high-cadence samples of the horizon value of $\dot{M}$ sampled with a time interval $\Delta t = 1$. For a Sgr A*-like mass of $4.3 \times 10^6\ M_\odot$, this corresponds to a sampling period of 21 s.

We construct the power spectrum of the time series using Welch's method for overlapping segments of time durations ranging from 2^7 (used to calculate a smooth spectrum at high frequencies) to 2^{15} (used at low frequencies), applying a Hann window to each segment. An overall linear trend in the quantities $\log t$ and $\log \dot{M}$ is subtracted before calculating each spectrum. We do this for the union of chunks 6 and 7. The

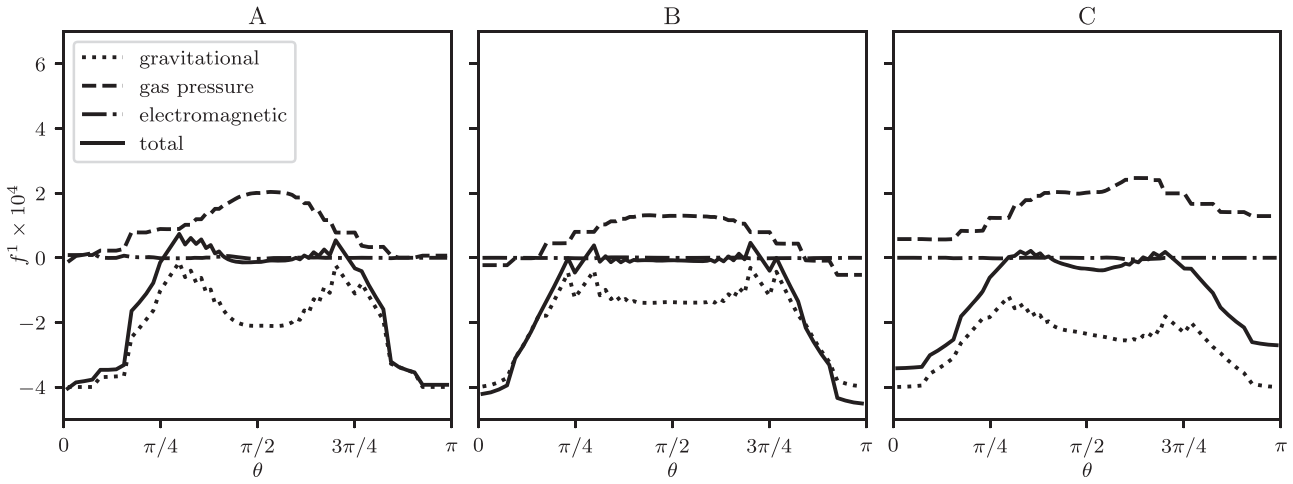

Figure 14. Forces acting in the radial direction (see Equation (16)) for a slice at $r = 50$, calculated in the fifth time chunk ($1.556 \times 10^5 \leqslant t < 2.2 \times 10^5$). The balance of forces is similar in all cases, with a disk supported by rotation and gas pressure and with inward accelerations at high latitudes.

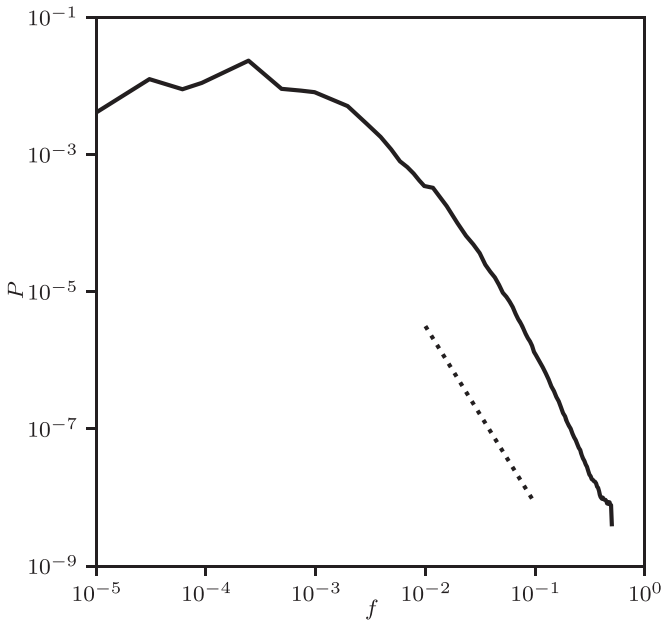

Figure 15. Power spectrum for time series of $\dot{M}$ at the horizon in simulation A. The data are taken from Chunks 6–7, covering $2.2 \times 10^5 \leqslant t \leqslant 4.4 \times 10^5$. The dotted line shows a slope of −2.59, which fits the spectrum over the indicated range.

results are shown in Figure 15. Here we refer to $P = fP_f$ as the power, where P_f is the power per unit frequency.

The spectrum has a slope $d \log P/d \log f \sim -2.59$ over the range $10^{-2} \leqslant f \leqslant 10^{-1}$, somewhat steeper than ideal red noise. The slope is −2.38 if we analyze chunks 1–5 instead of 6 and 7. A turnover to a flat spectrum is apparent at approximately $f = 10^{-3}$, especially in simulation A. Simulations B and C have similar spectra at low frequencies, both in amplitude and slope. However, their $\dot{M}$ values are only sampled every 100 time units, so we cannot measure their spectra at frequencies above 5×10^{-3}.

Numerical models of RIAFs have been widely used to predict event-horizon-scale emission and images. Such models form the basis for interpreting Event Horizon Telescope images of M87 (The Event Horizon Telescope Collaboration 2019a, 2019b, 2019c) and Sgr A*. Since our simulations provide three different realizations of the near-horizon structure of RIAFs, it is valuable to assess whether their predictions for the near-horizon emission differ. To do so, we employ the code `ibothros` (Noble et al. 2007) to generate images of synchrotron emission at 230 GHz in post-processing. We take 644 snapshots from chunk 5, separated by $\Delta t = 100$. For each one, we assume thermal synchrotron radiation from the electrons, with a simulation-to-electron temperature ratio of 4. The density scale of the simulation is adjusted to match the observed flux of 2.4 Jy of Sgr A* (Doeleman et al. 2008), assuming we are viewing the disk edge-on.

Figure 16 displays the average image resulting from stacking the 644 frames for each model. Simulation A shows the most extended disk component outside the typical bright ring around the circular dark region. This equatorial component is most compact in simulation C, brightening the ring but not increasing its width on the approaching side of the disk. These differences can be understood via the average density and temperature structures in the flows. Case C has the steepest density profile in the inner region (Figure 8), as well as higher temperatures (as can be seen in the larger scale height, Figure 7). Thus, the emission we see will be dominated by a small region near the photon orbit, slightly spread out along the ring but not radially. In contrast, case B and especially case A have emission from a wider range of radii near the disk midplane.

7. Conclusion

We have run and analyzed three long-timescale simulations of RIAFs around nonspinning black holes. Building on Narayan et al. (2012; see also related hydrodynamic work by Yuan et al. 2012) our goal has been to understand whether a well-defined self-similar structure of the accretion flow develops that is independent of the simulation initial conditions, and whether such a state is described by existing analytic models of RIAFs. All of our simulations are "SANE," i.e., they do not have significant net magnetic flux over an appreciable range of radii. We run a fiducial simulation (A) with small alternating field loops (see Figure 2) and adiabatic index $\Gamma = 4/3$ to $t = 4.4 \times 10^5$. Variations with either larger loops

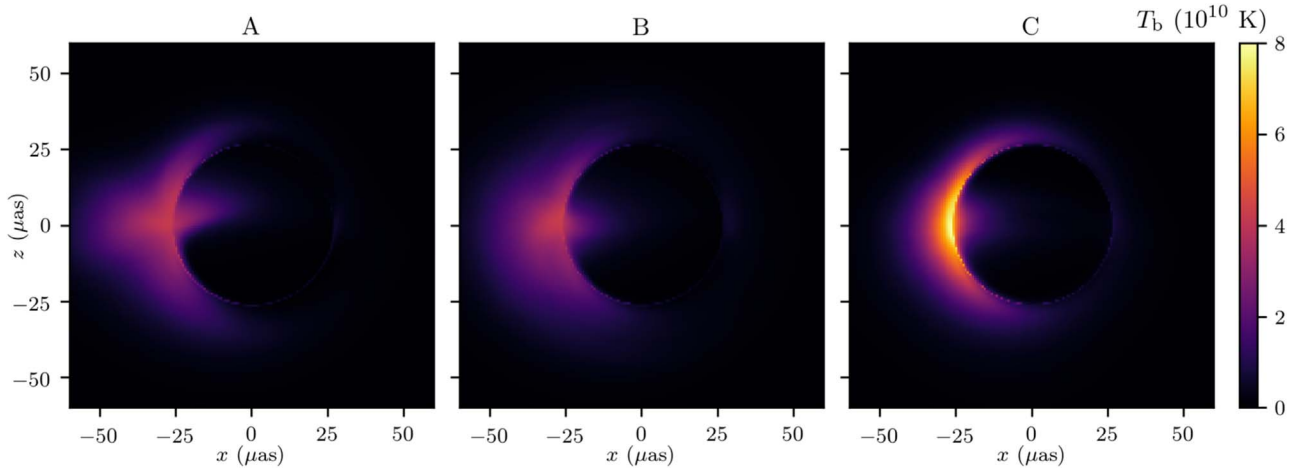

Figure 16. Images of the average 230 GHz thermal synchrotron emission from the three simulations, modeled using parameters appropriate for an edge-on view of Sgr A*. Simulations A and B have images more dominated by the equatorial disk, while simulation C shows a more prominent photon ring. This is a consequence of the differences in the scale heights and density profiles of these simulations (Figures 7 and 8). All three images have the same total flux.

(B) or $\Gamma = 5/3$ (C) are run to $t = 2.2 \times 10^5$. Note that $\Gamma = 4/3$ and $\Gamma = 5/3$ are rough approximations to super- and sub-Eddington RIAFs, respectively. The simulations reach inflow equilibrium, defined here as where $\dot{M}$ falls to $e^{-1/2}$ of its horizon value, past $r = 370$, $r = 170$, and $r = 440$, respectively. Energy and angular momentum fluxes are as constant with radius as mass fluxes over much of this range. We note that many of our principal conclusions are not unique to these long-timescale runs. On the contrary, Appendix B shows that they hold even for the smaller tori typically used in GRMHD simulations.

One of our principal results is that the dynamical structure of RIAFs is sensitive to initial conditions, at least over the time- and length-scales that we can afford to simulate. There is no evidence for a unique flow structure that loses memory of the initial conditions. This is not necessarily surprising given the lack of timescale separation among thermal, viscous, and dynamical times in RIAFs. Moreover, the absence of radiative cooling implies that the dynamics in RIAFs are particularly sensitive to modest changes in flow energetics (produced, e.g., by differences in magnetic field structure).

In more detail, Figure 8 shows that the $\Gamma = 4/3$ simulations maintain shallow slopes in density of $d \log \langle \rho \rangle / d \log r \approx -1/2$ in the innermost regions, with slopes at least as steep as approximately $-3/2$ in the outer regions that are still in steady state. In the $\Gamma = 5/3$ case, we see slopes closer to -1 in the inner regions and $-1/2$ in the outer regions. In a given simulation, we find that there is no clear convergence of $d \log \langle \rho \rangle / d \log r$ to a particular value in the steady-state flow exterior to the inner $10 - 30\ GM/c^2$, as might be expected if there were a unique self-similar solution for the structure of RIAFs. By contrast, such a well-defined radial profile is seen in hydrodynamic α models of RIAFs (e.g., Stone et al. 1999; Yuan et al. 2012). It is unclear if this difference between the hydrodynamic and MHD models reflects the very different angular momentum and energy transport physics in the two different simulations or if our simulations still do not have sufficient dynamic range to reach a quasi-self-similar state. We suspect the former.

The larger magnetic field loops in simulation B relative to simulation A (see Figure 2) result in the buildup of coherent magnetic flux at the horizon. While this simulation does not stay in a MAD state, it shows signs of alternating between "semi-MAD" states with oppositely directed fluxes. This does not have a noticeable effect on radial profiles of scale height, density, or magnetization, but it can affect the velocity structure of the accretion flow. In particular, the coherent vertical flux is enough to drive polar outflows in simulation B, whereas both simulations A and C have polar inflows of material (Figure 11). The absence of polar outflows in simulation C is particularly striking. as the density profile becomes nearly spherical with a density contrast of only a factor of a few between the equator and poles (Figure 10).

The polar inflows we find are not readily explained by models for convective stability or meridional circulation (see Appendix A). However even a small amount of inflow can release enough energy to unbind significant portions of the disk, which for RIAFs is at best marginally bound. This is likely why the flow structure is sensitive to the magnetic field initial conditions, since the latter influences the angular momentum and energy transport at essentially all times in the simulation. Overall, we find that unbound outflows change the horizon-scale accretion rate by only a factor of order unity relative to the accretion rate at $r \sim 300$ (see Figure 12), consistent with Narayan et al. (2012).

The sensitivity of the flow structure and dynamics in our simulations to modest changes in initial conditions (all within the context of highly artificial initial conditions) suggests that there is likely to be significant variation in the properties of RIAFs in nature depending on exactly how matter is supplied to the vicinity of the black hole from larger radii. Understanding this better in future work would be very valuable and would impact problems as diverse as accretion in the Galactic Center from stellar winds (e.g., Ressler et al. 2018) to the growth of supermassive black holes by highly super-Eddington accretion (e.g., Begelman & Volonteri 2017). We note that our calculations assume a nonspinning black hole, and future work should explore whether spin exacerbates or mitigates the sensitivity to how matter is supplied.

Numerical models of RIAFs have been widely used to predict event-horizon-scale emission, variability and images, particularly in the context of the well-studied systems M87 (e.g., Dexter et al. 2012; Mościbrodzka et al. 2016, 2017; Ryan et al. 2018; Chael et al. 2019) and Sgr A* (e.g., Mościbrodzka et al. 2014; Ressler et al. 2017; Chael et al. 2018). As a result,

we have made preliminary attempts to understand the observational implications of the diversity of flow structure and dynamics we find in our RIAF simulations. Toward this end, we calculate the power spectrum of $\dot{M}$ in time for simulation A, using high-cadence samples at time intervals of 1 GM/c^3 (21 s for $M = 4.3 \times 10^6\ M_\odot$), shown in Figure 15. The spectral power goes as $P \sim f^{-2.59}$ at high frequencies. Our data shows a turnover toward white noise (f^0) at low frequencies; such a turnover has been measured in the submillimeter emission of Sgr A*, occurring at a timescale of $\tau \approx 8$ hr (Dexter et al. 2014). This timescale corresponds to a frequency in our geometric units of $f = 7 \times 10^{-4}$ (for reference, this is the reciprocal of the orbital period at $r = 36$), which is consistent with where we see the turnover in $\dot{M}$ power.

Motivated by the Event Horizon Telescope, we also calculate millimeter images of synchrotron emission for parameters appropriate for Sgr A* (see Figure 16). All of our different realizations of RIAFs produce qualitatively similar images, dominated by a Doppler boosted region along with a faint ring (Figure 16). There are, however, interesting differences in the size of the emitting region and the prominence of the equatorial accretion disk, which is much less dominant in simulation C ($\Gamma = 5/3$) relative to simulations A and B ($\Gamma = 4/3$).

We thank all of the members of the Horizon Collaboration (http://horizon.astro.illinois.edu) for useful discussions. We thank J. M. Stone for valuable comments on the manuscript. This research was supported in part by the National Science Foundation under grants NSF PHY-1748958, NSF AST 13-33612, and NSF AST 1715054; by *Chandra* theory grant TM7-18006X from the Smithsonian Institution; and by a Simons Investigator award from the Simons Foundation (EQ). This work used the Extreme Science and Engineering Discovery Environment (XSEDE) Stampede2 at the Texas Advanced Computing Center through allocation AST170012, as well as the Savio computational cluster resource provided by the Berkeley Research Computing program at the University of California, Berkeley.

Software: `Athena++` (White et al. 2016), `ibothros` (Noble et al. 2007).

Appendix A
Analysis of Convection and Meridional Circulation

One possible cause of bulk outflows in disks is a stationary convection pattern. As described in Quataert & Gruzinov (2000) we can check for convective stability in the disk by examining the gradients of entropy $s \equiv \log(p_{\rm gas}\rho^{-\Gamma})$ and azimuthal velocity $v^\phi \equiv r\sin(\theta)u^3/u^0$. We construct the quantity

$$Q_{\rm conv} = r^6(C^2 - 4AB), \tag{17}$$

where A, B, and C are defined by (A2–A4) of Quataert & Gruzinov, using density-weighted averages of s and v^ϕ in time and azimuth and using the last time chunk $1.556 \times 10^5 \leqslant t < 2.2 \times 10^5$ available to all simulations. Stability requires $Q_{\rm conv} < 0$. The values for $Q_{\rm conv}$ within one scale height of the midplane are shown in Figure 17. The two simulations with disk outflows, A and C, are slightly unstable against convection in the midplane, in contrast to simulation B, which is marginal. However, simulation C is quite stable at slightly higher latitudes, where there is still a strong outflow. Thus, convection does not seem to fully explain the different bulk patterns shown in Figure 11.

Classical convection is not the only way to achieve large-scale motions in a disk. A sufficiently small vertical stratification in entropy can lead to meridional circulation in which the material in the midplane of the disk moves outward, with inward flow through the coronal layers. Following the constant $\dot{M}$ case presented in Philippov & Rafikov (2017) we define the circulation parameter

$$Q_{\rm circ} \equiv -\frac{\Gamma}{\delta_\rho + \delta_T}\left(3 + \frac{3\Gamma + 2}{2\Gamma}\delta_T + \frac{1-\Gamma}{\Gamma}\delta_\rho\right) - R^3\left(\frac{p_{\rm gas}}{\rho}\right)^2\frac{\partial^2 s}{\partial z^2}, \tag{18}$$

where δ_q denotes $\partial \log q/\partial \log R$. If this is positive we expect outflow in the midplane. $Q_{\rm circ}$ is plotted for the same time chunks in Figure 18. In all three cases the values are positive throughout the disk. However, the values are similar for all three simulations; thus if this were the cause of the outflows in simulations A and C, we would expect it to lead to the same velocity structure in simulation B, which is not seen.

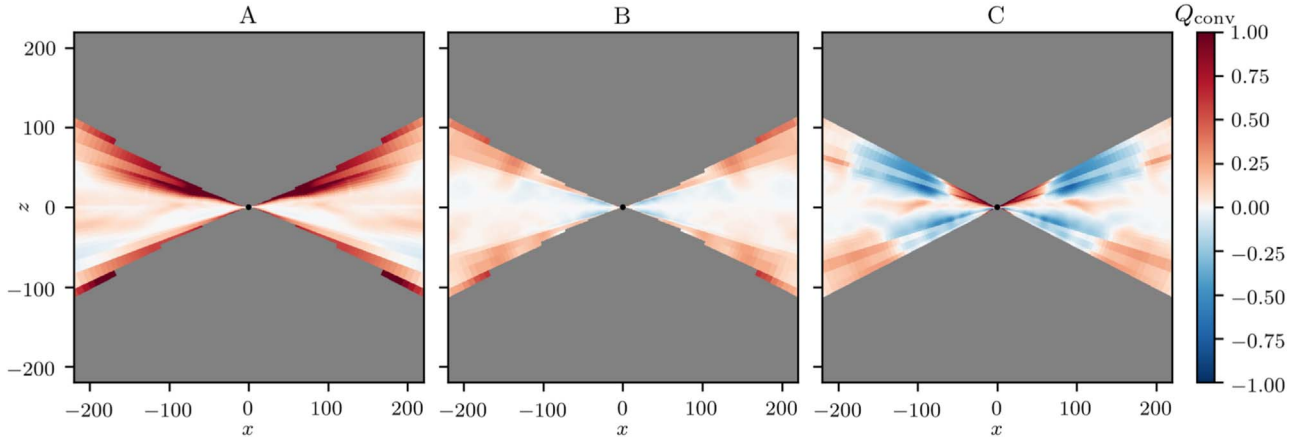

Figure 17. Convective stability measure $Q_{\rm conv}$ (Quataert & Gruzinov 2000) within one scale height of the midplane for the fifth time chunk ($1.556 \times 10^5 \leqslant t < 2.2 \times 10^5$) of each simulation. Convection is expected for positive values. While simulations A and C show outflows in the disk, they are no less stable than simulation B.

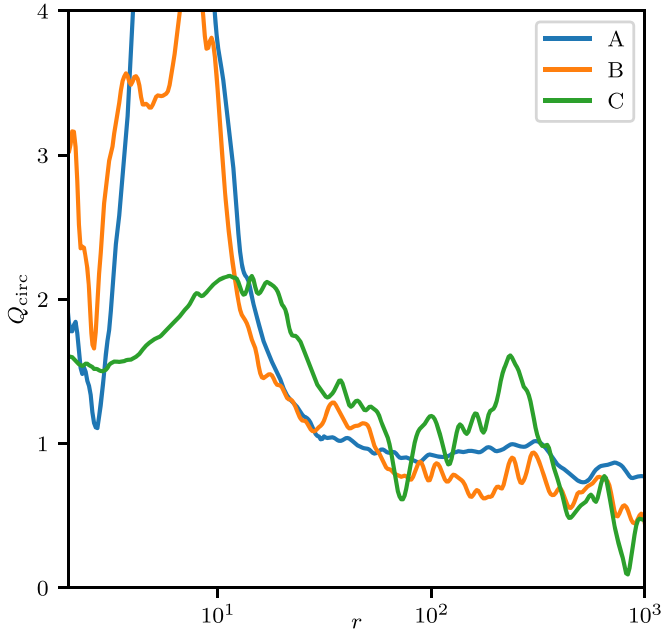

Figure 18. Meridional circulation criterion (Philippov & Rafikov 2017) calculated in the midplane for the fifth time chunk ($1.556 \times 10^5 \leqslant t < 2.2 \times 10^5$) of each simulation. Positive values predict a circulation pattern with outflow in the midplane. The values are positive everywhere, but they are roughly the same for all three simulations, whereas the simulations have different behaviors.

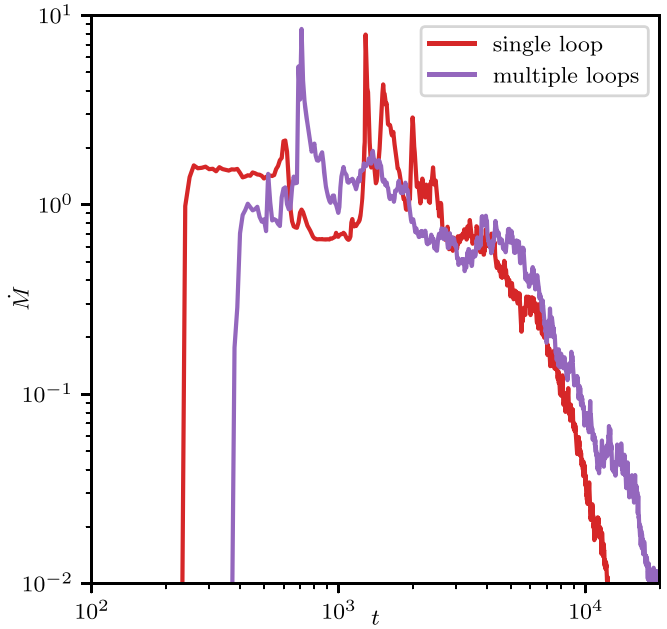

Figure 19. Horizon accretion rates as functions of time for the two small tori. The case with a single loop is a nonspinning analogue of the standard torus used to test and compare GRMHD codes as in Porth et al. (2019).

Appendix B
Comparison with Smaller Tori

Here we briefly mention two additional setups that are run for comparison. These two variants on the same small initial torus show how slight changes in the initial magnetic field can lead to different velocity structures in steady state.

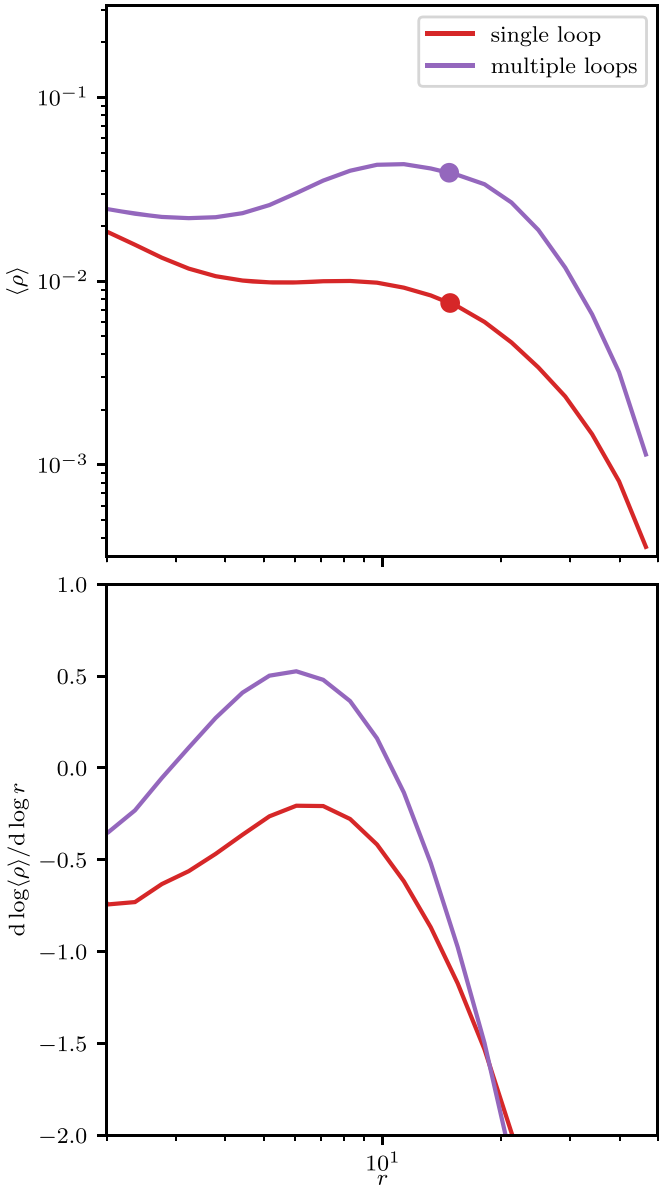

Figure 20. Radial density profiles and their power-law slopes for the small tori, averaged in time over $8000 \leqslant t \leqslant 10{,}000$. The points are at the same viscous radii as in Figure 19. The single-loop and multiple-loop variants are not too dissimilar from simulations B and A (their closest analogues) insofar as their slopes in the inner regions are shallower than the value of -1 seen in simulation C.

In both cases we start with a Fishbone & Moncrief (1976) torus around a nonspinning black hole with inner edge $r = 9$, pressure maximum $r = 17$, peak density $\rho = 1$, and adiabatic index $\Gamma = 4/3$. The grid extends inside the horizon and out to $r = 50$. At root level it contains 24^3 cells, and we add three successive levels of mesh refinement, obtaining an effective resolution of 192^3 within 37.5° of the midplane.

The single-loop variant has a magnetic field initialized via

$$A_\phi \propto \max(\rho - 0.2, 0), \tag{19}$$

while the multiple-loop variant employs (2) with $p_{\rm gas,min} = 10^{-8}$, $r_{\rm min} = 10$, $r_{\rm max} = 35$, $\theta_{\rm min} = 7\pi/18$, $\theta_{\rm max} = 11\pi/18$, $N_r = 3$, and $N_\theta = 2$. In both cases the normalization is such that the density-weighted average of β^{-1} is 10^{-2}, and we perturb the initial state via (5) with $\Delta_0 = 0.02$ and k_R, $k_z = 2\pi/5$.

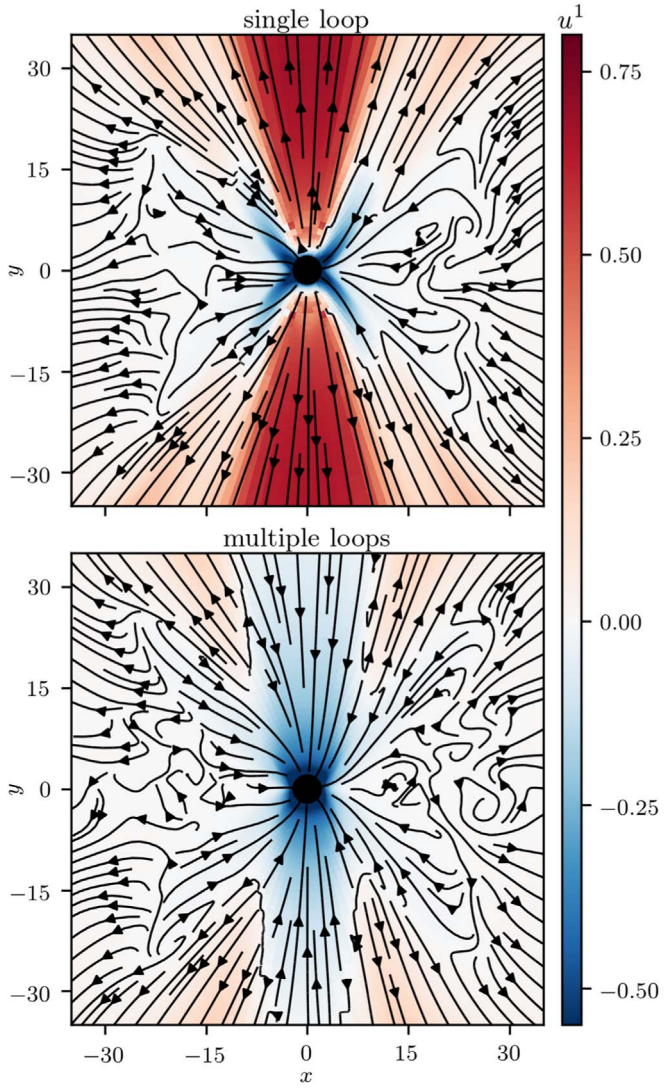

Figure 21. Average steady-state ($8000 \leqslant t \leqslant 10{,}000$) poloidal velocity fields for the small tori. As in Figure 11, the background color highlights radial velocity. The single-loop and multiple-loop variants resemble simulations B and A, respectively, in the polar region.

The single-loop variant is comparable to standard tori widely used in the literature when, for example, testing and demonstrating a new GRMHD code (Gammie et al. 2003; Antón et al. 2006; White et al. 2016; Porth et al. 2017) or comparing such codes (Porth et al. 2019), though around a nonspinning black hole here. It is similar to a scaled-down version of simulation B. The other small torus is more akin to a scaled-down version of simulation A. The only difference between the two is the magnetic field configuration, which is chosen to remain SANE in both cases.

Due to their small size, we can run these tori through steady state and even through depletion (by $t = 15{,}000$ for the single-loop case, slightly later with multiple loops) with relatively little computational expense. Figure 19 shows the run of $\dot{M}$ with time in both cases.

Even with these widely used, standard, small tori, the final density and velocity structures depend on the details of the initial field configuration. Density profiles, analogous to Figure 8, are shown in Figure 20, averaged in time over $8000 \leqslant t \leqslant 10{,}000$. Figure 21 shows the corresponding velocity structure, analogous to Figure 11. With a single loop, a relatively strong polar outflow is driven, even though there is no black hole spin, nor is a MAD state obtained. This reflects the behavior of simulation B, where some net vertical flux proves to be sufficient for launching polar outflows. On the other hand, the multiple-loop variant follows simulation A in having polar inflow at all radii.

The midplane in the multiple-loop small torus does not experience the same bulk outflow as simulation A. However, this can be attributed to larger Fishbone & Moncrief tori being less bound. The polar inflows in simulation A could unbind most of the accretion disk, while the inner parts of the multiple-loop disk can still flow inward despite the liberation of gravitational potential energy nearby.

ORCID iDs

Eliot Quataert https://orcid.org/0000-0001-9185-5044
Charles F. Gammie https://orcid.org/0000-0001-7451-8935

References

Antón, L., Zanotti, O., Miralles, J. A., et al. 2006, ApJ, 637, 296
Beckwith, K., Hawley, J. F., & Krolik, J. H. 2008, ApJ, 678, 1180
Begelman, M. C., & Volonteri, M. 2017, MNRAS, 464, 1102
Blandford, R., & Payne, D. 1982, MNRAS, 199, 883
Blandford, R., & Znajek, R. 1977, MNRAS, 179, 433
Blandford, R. D., & Begelman, M. C. 1999, MNRAS, 303, L1
Bondi, H. 1952, MNRAS, 112, 195
Chael, A., Narayan, R., & Johnson, M. D. 2019, MNRAS, 486, 2873
Chael, A., Rowan, M., Narayan, R., Johnson, M., & Sironi, L. 2018, MNRAS, 478, 5209
Chakrabarti, S. K. 1985, ApJ, 288, 1
Dexter, J., Kelly, B., Bower, G. C., et al. 2014, MNRAS, 442, 2797
Dexter, J., McKinney, J. C., & Agol, E. 2012, MNRAS, 421, 1517
Doeleman, S. S., Weintroub, J., Rogers, A. E., et al. 2008, Natur, 455, 78
Fishbone, L. G., & Moncrief, V. 1976, ApJ, 207, 962
Gammie, C. F., McKinney, J. C., & Tóth, G. 2003, ApJ, 589, 444
Hawley, J. F., & Balbus, S. A. 2002, ApJ, 573, 738
Ichimaru, S. 1977, ApJ, 214, 840
Igumenshchev, I. V., & Abramowicz, M. A. 2000, ApJS, 130, 463
Kozłowski, M., Jaroszyński, M., & Abramowicz, M. 1978, A&A, 63, 209
Mignone, A. 2014, JCoPh, 270, 784
Mignone, A., Ugliano, M., & Bodo, G. 2009, MNRAS, 393, 1141
Mościbrodzka, M., Dexter, J., Davelaar, J., & Falcke, H. 2017, MNRAS, 468, 2214
Mościbrodzka, M., Falcke, H., & Shiokawa, H. 2016, A&A, 586, A38
Mościbrodzka, M., Falcke, H., Shiokawa, H., & Gammie, C. F. 2014, A&A, 570, A7
Narayan, R., Igumenshchev, I. V., & Abramowicz, M. A. 2000, ApJ, 539, 798
Narayan, R., Igumenshchev, I. V., & Abramowicz, M. A. 2003, PASJ, 55, L69
Narayan, R., Mahadevan, R., Grindlay, J. E., Popham, R. G., & Gammie, C. 1998, ApJ, 492, 554
Narayan, R., Sądowski, A., Penna, R. F., & Kulkarni, A. K. 2012, MNRAS, 426, 3241
Narayan, R., & Yi, I. 1994, ApJL, 428, L13
Narayan, R., & Yi, I. 1995, ApJ, 452, 710
Noble, S. C., Leung, P. K., Gammie, C. F., & Book, L. G. 2007, CQGra, 24, S259
Penna, R. F., Kulkarni, A., & Narayan, R. 2013, A&A, 559, A116
Philippov, A. A., & Rafikov, R. R. 2017, ApJ, 837, 101
Porth, O., Chatterjee, K., Narayan, R., et al. 2019, ApJS, 243, 26
Porth, O., Olivares, H., Mizuno, Y., et al. 2017, ComAC, 4, 1
Quataert, E., & Gruzinov, A. 2000, ApJ, 539, 809
Rees, M., Begelman, M., Blandford, R., & Phinney, E. 1982, Natur, 295, 17
Ressler, S., Quataert, E., & Stone, J. 2018, MNRAS, 478, 3544
Ressler, S., Tchekhovskoy, A., Quataert, E., & Gammie, C. 2017, MNRAS, 467, 3604
Ryan, B. R., Ressler, S. M., Dolence, J. C., Gammie, C., & Quataert, E. 2018, ApJ, 864, 126

Shakura, N., & Sunyaev, R. 1973, A&A, 24, 337
Stone, J. M., Pringle, J. E., & Begelman, M. C. 1999, MNRAS, 310, 1002
Tchekhovskoy, A., Narayan, R., & McKinney, J. C. 2011, MNRAS, 418, L79
The Event Horizon Telescope Collaboration 2019a, ApJL, 875, L1
The Event Horizon Telescope Collaboration 2019b, ApJL, 875, L5
The Event Horizon Telescope Collaboration 2019c, ApJL, 875, L6
White, C. J., Stone, J. M., & Gammie, C. F. 2016, ApJS, 225, 22
Yuan, F., Wu, M., & Bu, D. 2012, ApJ, 761, 129